Title

Imaging Orientation of a Single Molecular Hierarchical Self-Assembled Sheet: The Combined Power of a Vibrational Sum Frequency Generation Microscopy and Neural Network

Journal

The Journal of Physical Chemistry B, 126(37)

ISSN

1520-6106

Authors

Wagner, Jackson C
Wu, Zishan
Wang, Haoyuan
et al.

Publication Date

2022-09-22

DOI

10.1021/acs.jpcb.2c05876

Peer reviewed

THE JOURNAL OF PHYSICAL CHEMISTRY B
A JOURNAL OF THE AMERICAN CHEMICAL SOCIETY

pubs.acs.org/JPCB

Article

Imaging Orientation of a Single Molecular Hierarchical Self-Assembled Sheet: The Combined Power of a Vibrational Sum Frequency Generation Microscopy and Neural Network

Published as part of The Journal of Physical Chemistry virtual special issue "Hiro-o Hamaguchi Festschrift".

Jackson C. Wagner,[⊥] Zishan Wu,[⊥] Haoyuan Wang, and Wei Xiong*

Cite This: *J. Phys. Chem. B* 2022, 126, 7192−7201

Read Online

ACCESS | Metrics & More | Article Recommendations | Supporting Information

ABSTRACT: In this work, we determined the tilt angles of molecular units in hierarchical self-assembled materials on a single-sheet level, which were not available previously. This was achieved by developing a fast line-scanning vibrational sum frequency generation (VSFG) hyperspectral imaging technique in combination with neural network analysis. Rapid VSFG imaging enabled polarization resolved images on a single sheet level to be measured quickly, circumventing technical challenges due to long-term optical instability. The polarization resolved hyperspectral images were then used to extract the supramolecular tilt angle of a self-assembly through a set of spectra-tilt angle relationships which were solved through neural network analysis. This unique combination of both novel techniques offers a new pathway to resolve molecular level structural information on self-assembled materials. Understanding these properties can further drive self-assembly design from a bottom-up approach for applications in biomimetic and drug delivery research.

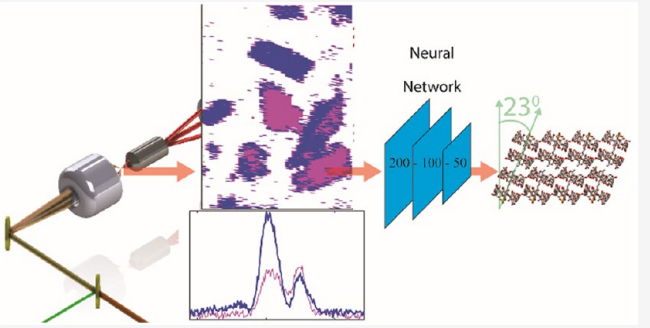

INTRODUCTION

Molecular self-assemblies (MSAs) are a class of materials that spontaneously organize from individual molecular subunits into an ordered structure without templates or external guidance.[1−6] MSAs can have larger architectures that maintain the high ordering and orientation of the smaller structures, known as hierarchical organization.[2,6−10] In both natural and synthetic materials, even when formed from identical subunits, different hierarchical organization can lead to various material functions.[11,12] For example, the diverse structures of natural collagen enable them to assume different tissue functions such as bone, skin, etc.[13] In particular, bone possesses a 12-level hierarchical structure from collagen fibrils to the macroscopic fractal-like architectures, affording it both high stiffness and toughness, properties often considered mutually exclusive.[14] Moreover, liquid crystal displays show different optical properties based on the orientation of the building blocks.[15] Thus, it is feasible to design and manipulate materials functions through hierarchical organizations; however, to do so, it is necessary to understand and control the relative positions and orientations of the subunits within the MSAs.[16,17]

Specifically, the orientation of building blocks within a MSA is important to its functions. Applications can be found in chemistry, such as alkanethiol self-assembled monolayers, which are used as an active layer in molecular electronics. The tilting of the alkanethiol chains with respect to surface normal can open additional tunneling pathways and change interfacial dipole properties, altering the electron transport properties.[18−20] In biomaterials, mechanical properties often depend on the hierarchical subunit orientation. For example, the longitudinal modulus of nacre is higher than the transverse modulus because of oriented tiles in the hierarchical structures.[21] It has also been demonstrated that surface wettability is correlated with the tilting of subunits,[22] which could further affect protein adsorption and cell adhesion.[23]

An interesting, recent development in MSAs is a lattice self-assembly composed of β-cyclodextrin (β-CD) and sodium dodecyl sulfate (SDS) in a 2:1 ratio, formed through intermolecular forces, especially hydrogen bonds.[11] This MSA assumes a variety of morphologies depending on the concentration of SDS and β-CD in water. We will refer to this MSA as SDS@2β-CD herein. The primary subunit of the SDS@2β-CD self-assembly is the supramolecule comprised of

Received: August 17, 2022
Revised: August 30, 2022
Published: September 13, 2022

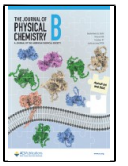

https://doi.org/10.1021/acs.jpcb.2c05876
J. Phys. Chem. B 2022, 126, 7192−7201

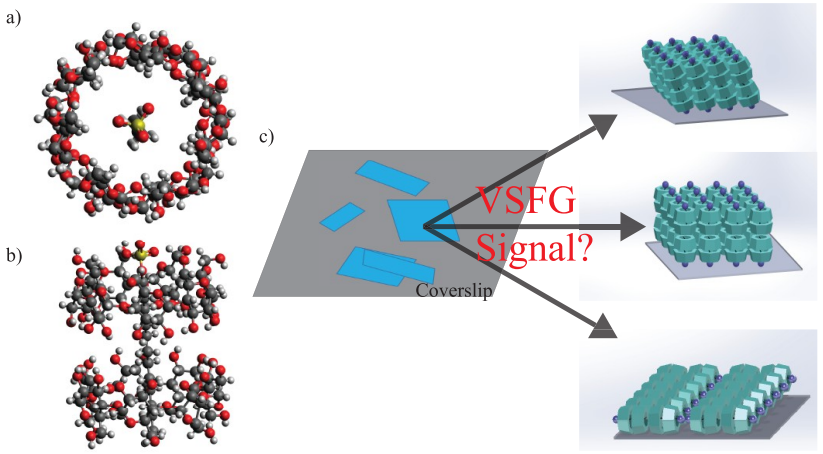

Figure 1. Structure of SDS@2β-CD. (a) Top down view of the SDS@2β-CD MSA subunits. (b) Side view of the subunits. (c) Microscopic formations of the SDS@2β-CD which hierarchically oriented to form rhombically shaped sheets. The orientation of the subunits relative to surface normal is unknown.

two β-CD molecules penetrated by one SDS molecule (Figure 1a,b). These subunits form highly ordered and oriented rhombic sheets that can fold into larger mesoscopic architectures such as, lamella sheets, microtubules, rhombic dodecahedra, and micelles, among others.[11] This MSA has drawn much attention because of the biomimetic nature of its mesoscopic architectures in addition to its broad application such as wastewater treatment,[24] drug delivery,[25] and optoelectronics.[26] However, the structural details of the subunits, the most basic formation of the self-assembly that folds into all other higher order molecular architectures, are not fully understood.[11] Through small-angle X-ray scattering (SAXS) the intersupramolecular distance was determined to be 1.52 nm, but open questions remain regarding the relative orientation of the subunits in SDS@2β-CD. Because molecular orientations often act as critical factors to MSA's functions, it is pertinent to understand whether and how the subunits in the self-assembled sheets are tilted (Figure 1c), which could potentially indicate the van der Waals contact, the structural symmetry, or the materials macroscopic properties.[18,22,27,28]

In this work, we determined the orientation of the subunits in SDS@2β-CD through the development of a fast line-scanning vibrational sum-frequency generation (VSFG) microscopy in combination with neural network data analysis.[29,30] Building on our previous efforts in ultrafast hyperspectral imaging techniques,[31,32] this new technical advancement enabled imaging single SDS@2β-CD sheets hyperspectrally with eight different polarization combinations. Then, to reveal structural information, we applied a neural network method to solve a set of equations that relate the supramolecular tilt angle to the second order susceptibility of different polarizations. We found that the subunits were tilted relative to normal of the sheets by ~23°. This provides insight into how to design future materials as well as offer details to what role hierarchical orientation played in MSAs. This structural knowledge is revealed through the combination of rapid acquisition of hyperspectral imaging and neural networks. Both are crucial to extract these parameters with the former minimizing long-term laser drift issues and the latter offering a route to solve a complex set of equations that were otherwise difficult to be solved.

METHOD

VSFG Line Scanning Microscope. The hyperspectral microscope was based on VSFG spectroscopy, a second-order nonlinear optical phenomenon. As an even-order nonlinear optical process, only noncentrosymmetric systems produce VSFG responses, such as the air/liquid, air/solid, and solid/liquid interfaces.[29,31−45] Furthermore, VSFG is also sensitive to materials without inversion centers,[46−55] many of which are MSAs, including collagen,[49,50] amyloid fibers,[56] artificial materials used in drug delivery,[57−59] metal−organic frameworks,[60−62] and piezoelectric crystals.[63]

A big challenge in using VSFG spectroscopy to probe MSAs is that most MSAs only form nano- to micrometer sizes domains, while the illumination area of VSFG spectroscopy is generally around 100 μm by 100 μm. Thus, traditional VSFG spectroscopy will probe multiple MSAs in an ensemble-averaged manner which does not accurately reflect the molecular structure of an individual MSA.[32] The development of VSFG spectroscopy into a hyperspectral imaging technique[32,48−50,52,53,64−67] overcame this challenge with 1 μm or submicrometer resolution being obtained, which offered a platform that could resolve multiple micrometer-sized MSAs individually.

Additionally, to retrieve molecular orientations, it was necessary to measure VSFG images with multiple polarization combinations.[49,50,65,68] Though theoretically feasible, it was practically prohibited in our previous point-scanning VSFG microscope[31,32] since it took nearly 4 h to scan a single 100 μm by 100 μm polarization resolved image and would take at least 30 h to collect all eight polarization combinations. The long acquisition time would introduce fluctuations in optomechanics and laser output, which further complicates data analysis.

To overcome these challenges, we hybridized the line-scanning technique with our existing VSFG microscope. A line-scanning method was first implemented in VSFG microscopy by the Ge and Potma groups using a photomultiplier tube as a detector,[49,50,64,65] which required scanning the IR frequency to gain spectral information. The integration of line-scanning with a CCD detector reported here enabled simultaneous measurement of spectra of a vertical line, maximizing the information measured by the 2D detector.

https://doi.org/10.1021/acs.jpcb.2c05876
J. Phys. Chem. B 2022, 126, 7192−7201

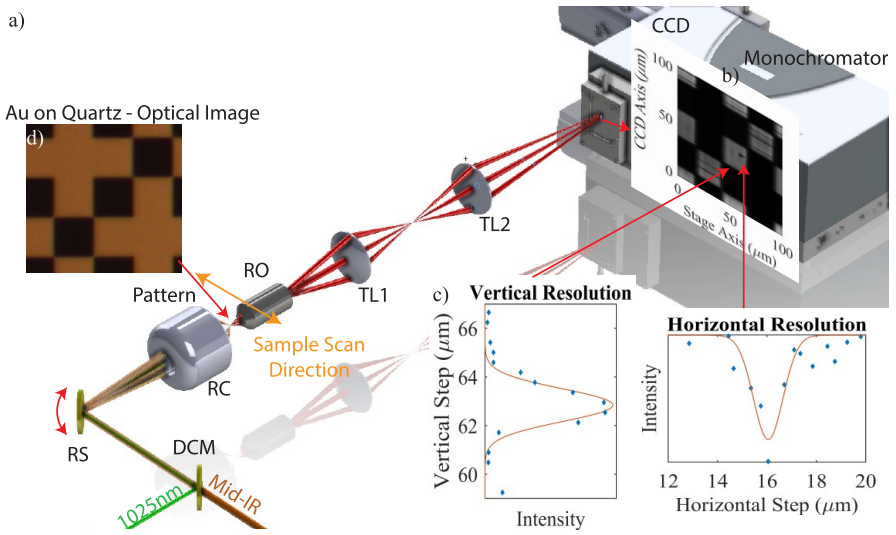

Figure 2. Line-scanning VSFG microscope. (a) Schematic of the setup: DCM, dichroic mirror; RS, resonant scanner; RC, reflective objective; RO, refractive objective; TL1, convex lens 1 in tube lens; TL2, convex lens 2 in tube lens. (b) VSFG image of quartz substrate target image. (c) Vertical and horizontal resolution generated by taking the derivative of the corresponding cut. The spectral resolution is 4 cm^{-1}. (d) Optical image of gold target on quartz substrate in a similar area.

The VSFG line-scanning microscope is shown in Figure 2. Laser pulses for the microscope are provided by a 100 kHz Yb based cavity femtosecond laser (Light Conversion, Carbide) centered at 1025 nm. The output from the Carbide is used to pump an optical parametric amplifier (OPA) (Light Conversion, Orpheus-HP) centered at 3500 nm which covers the CH stretching vibration region of interest. The residual 1025 nm beam is used as the up-conversion and is first conditioned spectrally by directing it through a folded 4f pulse shaper. The frequency narrowed 1025 nm beam is then focused through an 8 μm spatial filter followed by a $\lambda/2$ waveplate. The mid-IR (MIR) light is steered toward a delay stage followed by a $\lambda/2$ waveplate and spatially overlapped with the up-conversion with a customized dichroic mirror that is transparent to MIR and reflective to near IR (NIR). In this way, the mid-IR and upconversion beams are combined collinearly. The overlapped beams are then guided to a 1D resonant scanner (EOPC) and focused onto the sample mounted to a 2D piezo stage (MadCity Labs) by a purely reflective 20× Schwarzschild objective (0.70 NA, PIKE Technologies Inc., PN 891-0001). The emitted nonlinear VSFG signal is collected by an infinity corrected, 20× refractive microscope objective (Zeiss, Fluar 0.75 NA, working distance = 0.6 mm) and passes through a linear polarizer (ThorLabs). The polarization resolved signals are projected into spectra using a Shamrock 500i spectrograph (Andor) coupled to a CCD (Newton, Andor).

To enable line-scanning, the resonant scanner operated at 325 Hz and steered the angle of the beam along the vertical axis. At the sample plane, the incoming beams were transformed into a vertical line of illumination which generated a line of VSFG signal that was relayed and magnified by a home-built tube lens to match the vertical dimension of the CCD. The signal was frequency resolved by a spectrograph horizontally (Figure 2a). Thus, the CCD measured the spectra dispersed along the horizontal axis and the spatial profile along vertical axis. 2D images were acquired by scanning the sample in the horizontal direction with an automated mechanical stage. This improvement decreased image acquisition times by 10, compared to the point-by-point microscope, to 20 min for a 100 μm by 100 μm image.

The VSFG images obtained from the line-scanning microscope captured the same geometric features of the optical image of plated gold patterns on quartz substrates (Figure 2a,b,d). Depending on the scan angle of the resonant mirror and magnification of the tube lens, we achieved a 100 μm vertical field of view. The vertical and horizontal resolutions were 1.2 and 1.6 μm, respectively (Figure 2c), and the total magnification was 66.

2B-CD@SDS Synthesis. B-CD sheets are synthesized by adding B-CD and SDS at a molar ratio of 2:1 in DI water until the percent concentration is 10% m/m. The suspension is then heated to clarity and cooled to room temperature overnight. $CuCl_2$ is added with sheets fully forming approximately 3−5 days later. Isolated sheet samples with linear dimensions on the 10s of micrometer scale are produced by drop casting 5 μL of the sheet suspension onto a 15 mm × 15 mm × 0.170 mm microscope slide spinning at 10 000 rpm. The sheets are transparent, but the silhouette can be observed with a standard optical microscope.

Neural Network Model. The polarization dependent VSFG spectra were analyzed using a neural network model to extract molecular tilt information. Keras in Python is employed to set up the neural network model. A layered neural network modified from Github repotsitory[69] is built with a 200−100−50 node structure and a hyperbolic tangent activation function between layers (Figure 3). Training set with 100 000 by 27 values (see Supporting Information for details) was created by randomly generating angles and hyperpolarizabilities (used as training output, 100 000 by 11 values) and then supplying the values to the polarization-dependent equations (eqs 5−12 in Supporting Information) to calculate the corresponding susceptibilities (used as training input, 100 000 by 16 values) (Figure 3, Figure S13a). Similar to simple trigonometric function where $\theta = 0$ and $\theta = \pi$ both satisfy $\sin(\theta) = 0$, one input vector (susceptibility values) in our model could also have multiple output vectors (different in-plane rotation, tilt angle, hyperpolarizabilities combinations) at the same time.

https://doi.org/10.1021/acs.jpcb.2c05876
J. Phys. Chem. B 2022, 126, 7192−7201

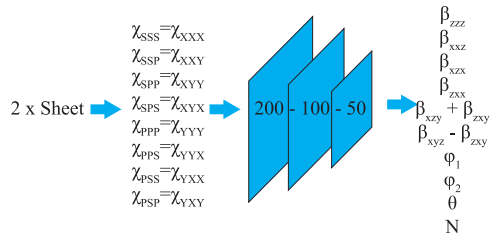

Figure 3. Schematic illustration of the neural network employed to extract orientation information on the SDS@2β-CD.

Hence, the in-plane rotation angle is divided into $[0, \pi)$ and $[\pi, 2\pi)$ intervals and the tilt angle is divided into $[0, \pi/2)$ and $[\pi/2, \pi)$ intervals to differentiate these output vectors. Training is run with an epoch size of 1000 and a batch size of 100. Mean squared error of output vector is used to monitor the deviation of prediction from true values. During the training, only 90% of the data set is used for actual modeling and the rest 10% of the training data is separated out to testify whether the model can generalize to unseen data. In such a way one can mitigate overfitting, as seen in the small and close loss values obtained in both training and test processes (Figure S13b).

After validating that our model is capable of predicting the tilt angle, we supply the model with experimentally determined susceptibilities Figures S9 and S10, Table S1) to extract the tilt angle. Since there is no phase information in our measurement, we enumerate the sign of each susceptibility value (total of 2^{16} combinations) and provide all these as input vectors to our neural network.

RESULTS AND DISCUSSION

Polarization Resolved Hyperspectral Imaging on SDS@2β-CD. To measure the tilt angle of subunits in SDS@2β-CD, we applied the line-scanning VSFG microscope to image single SDS@2β-CD sheets. Single SDS@2β-CD sheets, which can be visually seen under optical microscope with micrometer size, were carefully prepared (synthesis details in Supporting Information). We note that the single sheets are composed of multilayers of self-assembled materials instead of a monolayer, and its thickness is about 110 nm, determined by AFM height profiles (Figures S2 and S3). Via inspection with an optical microscope, we mitigate sheet overlapping, which would complicate analysis later as well as affect the image quality, by optimizing spin coating parameters (Figure S1).

An example of hyperspectral images of SSS polarization combination (left to right were polarization of VSFG, upconversion, and IR beams) was shown in Figure 4a. Edges of a single SDS@2β-CD sheet could be clearly seen as well as the rotational orientation of the rhombic shape inherent to the self-assembly, and the VSFG and optical images agreed well (Figure 4c,d). An atomic force microscope (AFM) was also used to image the sheets (Figure S2), and well separated single sheets are captured, with sharp edge contrast that is also seen by our VSFG microscope (Figure 4a). We noted that there was a significant improvement in the quality of VSFG images and their agreement with the optical images of the SDS@2β-CD, compared to the images in our previous publications.[31,32] This improvement is achieved by (1) an improved sample deposition method to prepare single sheets instead of multiple sheets overlapping on top of each other and (2) the fast line-scanning VSFG microscope that allowed optimizations of image quality within a short image acquisition time and large field of view, which was not available before.

To further disentangle spectral features of the VSFG image, spectral maps were generated using the MatLab hyperspectral imaging toolbox. Two unique spectra for the SSS polarization combination were identified, highlighted in blue and magenta in Figure 4a with corresponding spectra shown in Figure 4b. Clearly, there were two types of sheets and the sheets with

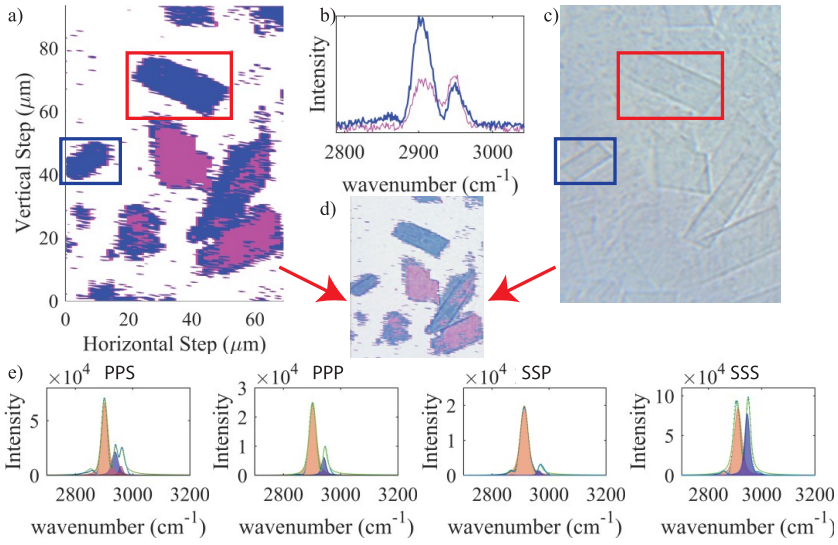

Figure 4. VSFG hyperspectral image and spectral analysis of the SDS@2β-CD. (a) Polarization resolved hyperspectral VSFG image of SDS@2β-CD. Blue and magenta colors represent areas where different spectra reside, and the corresponding spectra are plotted in (b) which are representative spectra for single pixels with signal-to-noise ratio for blue and magenta spectra of ~56 and ~26 respectively. The sheets in the red and blue boxes are analyzed explicitly below to extract the supramolecule tilt angles. (c) Optical image of the same area as that in (a). (d) VSFG hyperspectral image overlaid with optical image of identical area. (e) From left to right: PPS, PPP, SSP, SSS polarization resolved spectra summed over 180 and 480 pixels within the two single sheets highlighted in red rectangular boxes in (a). All spectra had a dominant feature centered at approximately 2910 cm^{-1} and a signal-to-noise ratio in the order of 1000. The spectra were fitted with multiple Voigt functions, which were represented by the shaded areas, and used for further orientation analysis.

https://doi.org/10.1021/acs.jpcb.2c05876
J. Phys. Chem. B 2022, 126, 7192−7201

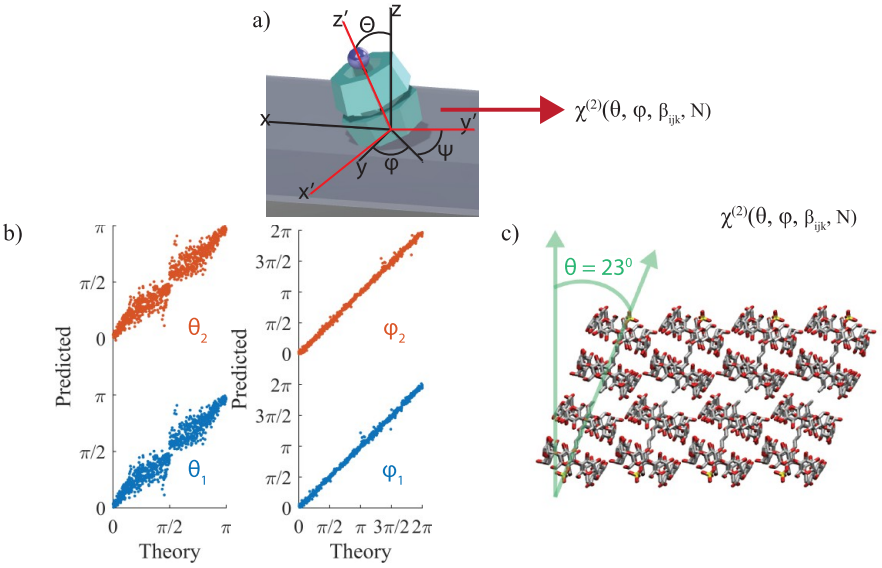

Figure 5. Euler transformation, neural network, and extracted tilt angles of the subunits in MSAs. (a) Euler transformation between the laboratory coordinates (*XYZ*) and the molecular coordinates (*xyz*). *z*−*y*′−*z*″ Euler rotation is performed on the molecular coordinates, with φ as the in-plane rotation angle, θ as the tilt angle, and ψ as the twist angle. (b) Neural network results for the tilt (left) and in-plane rotation (right) angles. (c) Visualization of the tilted subunits forming a sheet determined by the neural network results.

magenta color coding are due to sheet overlapping. In the following, we only analyze the areas highlighted with the red and blue rectangular boxes to extract tilt angles, which were single sheets identified using an optical microscope.

To extract molecular orientations, all eight lab frame VSFG polarization combinations (SSS, SSP, SPS, PSS, SPP, PSP, PPS, PPP) were collected. We summed spectra over all pixels within single sheets (pixel index shown in Figure S8), and four representative polarizations resolved VSFG spectra are shown in Figure 4e with a signal-to-noise level of 1000 (additional spectra shown in Figures S9 and S10). Each spectrum was fitted with multiple Voigt functions (shaded area, Figures 4e, S9, and S10, eq 13 in Supporting Information; detailed fitting parameters are summarized in Table S1). From the fitting, we have identified peaks at 2860 cm^{-1}, 2910 cm^{-1}, 2930 cm^{-1}, and 2960 cm^{-1} which can be assigned to the $-CH_2$ symmetric stretch, $-CH_2$ asymmetric stretch, $-CH_2$ Fermi resonance of p-polarized signals, and $-CH_2$ Fermi resonance of s-polarized signals.[70] In all spectra, we identified a clear peak at the 2910 cm^{-1} position, the $-CH_2$ asymmetric vibration, which we used for the orientation analysis below. The signal arises only from β-CD, as when using deuterated SDS to form *d*-SDS@2β-CD complex, the signal in this region is unchanged and no signal of deuterated CH_x were observed (Figures S5 and S6).[31] This observation is a result of the inherent chirality of β-CD which even as a dimer does not have an inversion center. Thus, the CH_x modes in β-CD are VSFG active. The CH_x modes in SDS, however, do not survive as SDS is achiral within the MSA.

Theoretical Basis of Orientation Analysis of a Single MSA Sheet. Theoretically, VSFG spectra with different polarization combinations, which were related to the lab frame second order susceptibility, $\chi^{(2)}_{IJK}$, could be expressed in terms of the molecular orientation (such as tilt angle and in-plane rotation) in the lab frame and molecular frame hyperpolarizability tensor, β_{ijk}, through an Euler rotation (Figure S7 and eqs 5−12).[49,65,71,72] In our measurement, the *z*-axis of the lab frame and the MSA frame were identical (i.e., sheets lying flat, but subunits may not), and the x-*y* axis of the MSA was only rotated away from their counterparts in the lab frame. Thus, in principle, we could extract the relative subunits orientation in the MSA using the lab frame VSFG spectral intensity.

Because the SDS@2β-CD supramolecule has C_7 symmetry, it has 13 β_{ijk} elements, of which only 7 are nondegenerate, β_{zzz},β_{xxz},β_{xzx},β_{zxx},β_{xzy},β_{zxy},β_{xyz} (eqs 1 and 2 in Supporting Information).[32] We note that these hyperpolarizabilities are contributed from all CH_2 asymmetric stretches of SDS@2β-CD supramolecule, so they together satisfy the C_7 symmetry of the supramolecules. In this way, it is not necessary to consider hyperpolarizability of individual CH_2 groups. Here, we also do not assume Kleinman symmetry, which has been previously reported as nonuniversal.[73,74] Then, for the lab frame, with the NA of the condenser objective being 0.7, the axial *z*-component can be neglected,[75] which renders 8 independent second order measurement $\chi^{(2)}_{XXX} = \chi^{(2)}_{SSS}$, $\chi^{(2)}_{XXY} = \chi^{(2)}_{SSP}$, $\chi^{(2)}_{XYX} = \chi^{(2)}_{SPS}$, $\chi^{(2)}_{YXX} = \chi^{(2)}_{PSS}$, $\chi^{(2)}_{XYY} = \chi^{(2)}_{SPP}$, $\chi^{(2)}_{YXY} = \chi^{(2)}_{PSP}$, $\chi^{(2)}_{YYX} = \chi^{(2)}_{PPS}$, $\chi^{(2)}_{YYY} = \chi^{(2)}_{PPP}$. Through an Euler rotation (Figures 5a and S7) and assuming the twist angle, ψ, is arbitrary, the lab frame $\chi^{(2)}$ could be expressed as a function of β_{ijk} and solid angles, resulting in a set of 8 equations (eq 5−12 in Supporting Information). One of the output equations of the Euler rotation is provided, eq 1, as an example and the rest were listed in the Supporting Information. As evident from eq 1 and Supporting Information eqs 5−12, three hyperpolarizability elements were not completely independent as they appeared as $\beta_{xzy} + \beta_{zxy}$ and $\beta_{xyz} - \beta_{xyz}$ grouped terms in all equations. Therefore, 7 nondegenerate hyperpolarizability elements were grouped down to 6 independent terms simplifying our set of 8 equations with 8 inputs to 8 unknowns (6 β_{ijk} grouped terms and two solid angles).

$$\chi^{(2)}_{PPS} = \frac{1}{16}[(4\cos(3\varphi)\sin^3(\theta) + \cos(\varphi)(13\sin(\theta) + \sin(3\theta))\beta_{xxz} - 8\sin(\varphi)(\sin(2\theta)(\beta_{xzy} + \beta_{zxy}) + \sin^3(\theta)\sin(2\varphi)(\beta_{xzx} + \beta_{zxx} - \beta_{zzz})) \quad (1)$$

https://doi.org/10.1021/acs.jpcb.2c05876
J. Phys. Chem. B 2022, 126, 7192−7201

To extract molecular orientations in the MSA frames, we need to solve the equations based on the experimentally measured $\chi^{(2)}$ to extract θ, φ, and β_{ijk}. To enhance the consistency of the result, we analyzed the signal on two single sheets and assumed that the supramolecular subunit in all single sheets had the same tilt angle. Two single sheets, i.e., without overlapping and with visibly different orientations, were selected as a simplified scenario (highlighted by red and blue boxes in Figures 4a and S8). The $\chi^{(2)}$ of the 2910 cm^{-1} peak of two sheets were extracted by the fitting results illustrated in Figures 4e, S10, and S11, for the orientation analysis. Based on the optical images, (Figures 4 and S8), we determined that the two single sheets are rotated approximately 60° in the *XY* plane relative to one another. Therefore, we further restrained our model with $\varphi_2 = \varphi_1 + 60$ degrees. As a result, for two sheets, we have 16 input known values (2×8 different polarization combinations) and 9 unknown outputs: 6 independent variables consisting of β_{ijk}, the in-plane rotation φ_1, tilt angle θ, and the relative coverage ratio N between sheets.

Neural Networks To Train the Solvers and Extract Tilt Angles. This equation set was solvable; however, traditional Matlab solver either provides no solution due to less tolerance to noise, which is always present in experimental data, or runs for a long time with 2^{16} sign enumerated combinations of input and 1000 iterations for each combination.[76,77] These limitations prohibited us from obtaining reasonable results, so we turned to a neural network approach (Figure S13).[69,78] A training set was used to train the neural network to identify relationships between the susceptibilities and molecular details (see Method and Supporting Information). To mitigate overfitting, i.e., the model memorizes training data well but cannot generalize relationships to new data it has never encountered, we use 10% of our training set as a validation set to monitor the model loss during training (Figure S13b). It is apparent that with more training cycles the model can predict with less deviation/loss from true values, and it can also predict the validation set which contains data not used for actual training relatively well. Therefore, with experimental results that are new input for the model too, it should be able to predict with a similar error level. To quantify the error and deviation of prediction, the trained model was then tested with another data set (1000 by 27 values) generated via a similar random process (Figure S13a). Figure 5b displayed the correlation between Euler angles, i.e., molecular orientations, predicted by our model which captured the true values in the test data set well, resembling a $y = x$ relationship with mean squared error of in-plane rotation prediction of 0.4° and that of tilt-angle at <30° region of 1.5°. Thus, our neural network based orientation solver was appropriate in predicting the molecular orientations.

Finally, we extracted molecular orientation using this method, by supplying it with the experimentally determined susceptibility values (Tables S1 and S2). Since phase information was not retrieved in our homodyne experiment, we enumerated the signs of all 16 susceptibility values when supplying them to the model and selected the predicted results with the smallest mean squared error of susceptibilities. By calculating the mean squared errors of the predicted normalized susceptibility values and the experimentally determined ones, the smallest mean squared error we can obtain is 0.02, whose corresponding predicted tilt angle away from the lab frame *z*-axis is 23 ± 1.5° (Supporting Information Table S2 and Figure 5c). To the best of our knowledge, this is the first work using neural network to relate VSFG spectral observables back to physical properties of molecules, while other studies involving machine learning in the SFG field mainly focus on assisting peak fitting/assignment and sole spectral analysis.[79−81]

From the polarization-dependent equations we could see that if the tilt angle was 0°, all susceptibility terms on the left side of the equations would be zero, which did not agree with the strong SFG signal, implying nonzero susceptibilities of the SDS@2β-CD system. On the other hand, using the literature reported in-plane unit cell parameters of the SDS@2β-CD system,[11] we could visually demonstrate that when the tilt angle was 30°, the space between subunits was tight, and when the tilt angle was 45−60°, SDS@2β-CD subunits would collide with each other (Figure S12). Hence, The results retrieved from the neural network mode, i.e., the SDS@2β-CD subunits were tilted slightly at 23 ± 1.5°, was appropriate and consistent with existing structural knowledge of the self-assembly. The tilt angle result is further validated when compared with results from X-ray diffraction. The XRD results indicate the stacking height of 4 SDS@2β-CD (a unit cell) to be 2.9 nm, while if the 4 SDS@2β-CDs sit straight up, their height should be 3.1 nm. To make the height to be 2.9 nm, an angle of approximately 20° is necessary (further explained in Supporting Information section I and Figure S4). Moreover, the AFM height profile shows a gradient height change across the edge and the edge incline/tilt toward sheet center, which could also be due to the stacking of tilted subunits. Comparable to the well-studied self-assembled monolayer on metal substrates, we believed the driving force of the tilting could be the interplay of intermolecular interactions (such as hydrogen bonds) among subunits and binding behaviors between subunits and substrate.[22,27,82,83]

It had been widely studied that the tilt of molecules within monolayers commonly existed in self-assembled materials and potentially adjusted the conduction,[84,85] wetting,[86,87] or mechanical properties.[84,88,89] With SDS@2β-CD as an important biomimetic motif, the tilt angle resolved in our neural network approach sheds light on how the subunits pack within the self-assembly and provides a protocol to study other MSA systems structure−properties correlations. For example, when the supramolecule units tilt, the top part of one unit overlaps with the bottom part of another unit, creating a fish scale type of structure, increasing the mechanical stability, compared to if the unit sits straight up. Moreover, as the tilting is influenced by the interaction of the subunits and hydration level, future works on humidity dependent packing of the system might unravel how the chemical environments affect the self-assembly process and could be very interesting and significant for the drug delivery field[90] as the release of target molecules highly relies on the biological environment.

It is noteworthy that such information is difficult to obtain with IR microscope. Based on the C7 symmetry of the SDS@2β-CD supramolecule, only μ_z is nonvanishing in molecular frame. The dipole moment in the lab frame can be expressed as a vector $(\cos\phi \sin\theta\mu_z \ \sin\phi \sin\theta\mu_z \ \cos\theta\mu_z)$ via the aforementioned Euler transformation. To extract tilt angle θ, we have to measure the *Z* component $\cos\theta\mu_z$ in the lab frame, which is practically difficult as it requires the incident IR beam to have a large polarization component along the surface normal. Furthermore, with 3 unknowns (φ, Θ, μ_z) and only 2 knowns (P and S polarizations of IR beam), it is an

https://doi.org/10.1021/acs.jpcb.2c05876
J. Phys. Chem. B 2022, 126, 7192−7201

underdetermined problem, which still requires the multisheet approach demonstrated in our neural network approach.

CONCLUSION

We note that there are a couple of limitations of the current microscope. First. The spatial resolution is only 1.6 μm, which limits its utility to imaging smaller domains. This limitation could be improved by using higher NA objective lens.[50] Second, the current sensitivity might not be able to image a self-assembled monolayer. This limitation is partly because the electromagnetic field projection on the z axis is too small, which always contributes strongly to the self-assembled monolayers. Thus, it is possible to image monolayers by tilting the sample relative to the beam propagation directions. However, it will detoriate the spatial resolution. Nevertheless, should these limitations be overcome, the present fast line-scanning and neural network analysis method can be readily applied. Indeed, the neural network analysis can be applied to any typical SFG spectroscopy study, when the orientation analysis becomes difficult.

The molecular self-assembly formed from a mixture of β-CD and SDS in water was analyzed using a line-scanning hyperspectral VSFG microscope and neural network. A 1D resonant scanner coupled to a CCD/spectrograph increases image collection speed 10-fold with simultaneous spectral information. This development enables polarization resolved VSFG images of single MSA sheets, which were analyzed by a neural network approach. The analysis revealed that the supramolecular subunits are tilted at around 23 $\pm$ 1.5° in the SDS@2β-CD MSA frame. Such information could help us further understand the structure and intermolecular interactions of other biomimetic morphologies that the subunits construct. This information became available because of the power of VSFG microscopy to extract spatially resolved, spectral information of the sheets.

ASSOCIATED CONTENT

Supporting Information

The Supporting Information is available free of charge at https://pubs.acs.org/doi/10.1021/acs.jpcb.2c05876.

Euler rotation and spectra fitting equations, XRD data, neural network details, spectra analysis with MATLAB hyperspectral imaging toolbox, and fitting results (PDF)

AUTHOR INFORMATION

Corresponding Author

Wei Xiong − *Department of Chemistry and Biochemistry, University of California San Diego, La Jolla, California 92093, United States; Materials Science and Engineering Program and Department of Electrical and Computer Engineering, University of California San Diego, La Jolla, California 92093, United States;* orcid.org/0000-0002-7702-0187; Email: w2xiong@ucsd.edu

Authors

Jackson C. Wagner − *Department of Chemistry and Biochemistry, University of California San Diego, La Jolla, California 92093, United States;* orcid.org/0000-0002-0703-7928

Zishan Wu − *Department of Chemistry and Biochemistry, University of California San Diego, La Jolla, California 92093, United States;* orcid.org/0000-0003-4810-9112

Haoyuan Wang − *Department of Chemistry and Biochemistry, University of California San Diego, La Jolla, California 92093, United States;* Present Address: Intel Corporation, Rio Rancho, NM 87124, Unites States; orcid.org/0000-0002-6226-6328

Complete contact information is available at: https://pubs.acs.org/10.1021/acs.jpcb.2c05876

Author Contributions

⊥J.C.W. and Z.W. contributed equally to this work.

Notes

The authors declare no competing financial interest.

ACKNOWLEDGMENTS

Z.W. and W. X. thank Prof. Sichun Gao's insightful discussion about neural network. W.X. thanks Prof. Hong-fei Wang for sharing his knowledge on the Klienmann symmetry. We thank Guoxin Yin and Chenglai Wang for performing FTIR and XRD measurements, and Deborah Kim from the Grassian group for taking the AFM and AFM-IR images. The instrument development is supported by Grant NSF CHE-1828666. Z.W. and J.C.W. are supported by National Institutes of Health, National Institute of General Medical Sciences, Grant 1R35GM138092-01.

REFERENCES

(1) Manchineella, S.; Govindaraju, T. Molecular Self-Assembly of Cyclic Dipeptide Derivatives and Their Applications. *Chempluschem* **2017**, *82* (1), 88−106.

(2) Yuan, C.; Ji, W.; Xing, R.; Li, J.; Gazit, E.; Yan, X. Hierarchically Oriented Organization in Supramolecular Peptide Crystals. *Nat. Rev. Chem.* **2019**, *3* (10), 567−588.

(3) Whitesides, G. M.; Mathias, J. P.; Seto, C. T. Molecular Self-Assembly and Nanochemistry: A Chemical Strategy for the Synthesis of Nanostructures. *Science* **1991**, *254* (5036), 1312−1319.

(4) Zhang, S. Fabrication of Novel Biomaterials through Molecular Self-Assembly. *Nat. Biotechnol.* **2003**, *21* (10), 1171−1178.

(5) Yi, R.; Mao, Y.; Shen, Y.; Chen, L. Self-Assembled Monolayers for Batteries. *J. Am. Chem. Soc.* **2021**, *143* (33), 12897−12912.

(6) Li, Z.; Cai, B.; Yang, W.; Chen, C.-L. Hierarchical Nanomaterials Assembled from Peptoids and Other Sequence-Defined Synthetic Polymers. *Chem. Rev.* **2021**, *121* (22), 14031−14087.

(7) Kulkarni, C. V. Lipid Crystallization: From Self-Assembly to Hierarchical and Biological Ordering. *Nanoscale* **2012**, *4* (19), 5779.

(8) Gerbelli, B. B.; Vassiliades, S. V.; Rojas, J. E. U.; Pelin, J. N. B. D.; Mancini, R. S. N.; Pereira, W. S. G.; Aguilar, A. M.; Venanzi, M.; Cavalieri, F.; Giuntini, F.; et al. Hierarchical Self-Assembly of Peptides and Its Applications in Bionanotechnology. *Macromol. Chem. Phys.* **2019**, *220* (14), 1900085.

(9) Ikkala, O.; ten Brinke, G. Hierarchical Self-Assembly in Polymeric Complexes: Towards Functional Materials. *Chem. Commun.* **2004**, No. 19, 2131.

(10) Ganewatta, M. S.; Wang, Z.; Tang, C. Chemical Syntheses of Bioinspired and Biomimetic Polymers toward Biobased Materials. *Nat. Rev. Chem.* **2021**, *5* (11), 753−772.

(11) Yang, S.; Yan, Y.; Huang, J.; Petukhov, A. V.; Kroon-Batenburg, L. M. J.; Drechsler, M.; Zhou, C.; Tu, M.; Granick, S.; Jiang, L. Giant Capsids from Lattice Self-Assembly of Cyclodextrin Complexes. *Nat. Commun.* **2017**, *8*, 15856.

(12) Gautieri, A.; Vesentini, S.; Redaelli, A.; Buehler, M. J. Hierarchical Structure and Nanomechanics of Collagen Microfibrils from the Atomistic Scale Up. *Nano Lett.* **2011**, *11* (2), 757−766.

(13) Birk, D. E.; Brückner, P. Collagens, Suprastructures, and Collagen Fibril Assembly. In *The Extracellular Matrix: An Overview*; Springer: Berlin, 2011; pp 77−115, DOI: 10.1007/978-3-642-16555-9_3.

(14) Reznikov, N.; Bilton, M.; Lari, L.; Stevens, M. M.; Kröger, R. Fractal-like Hierarchical Organization of Bone Begins at the Nanoscale. *Science* **2018**, *360* (6388), eaao2189.
(15) Castellano, J. A. *Liquid Gold*; World Scientific, 2005; DOI: 10.1142/5622.
(16) Feng, L.; Wang, K.-Y.; Day, G. S.; Zhou, H.-C. The Chemistry of Multi-Component and Hierarchical Framework Compounds. *Chem. Soc. Rev.* **2019**, *48* (18), 4823−4853.
(17) Caulder, D. L.; Raymond, K. N. Supermolecules by Design. *Acc. Chem. Res.* **1999**, *32* (11), 975−982.
(18) Frederiksen, T.; Munuera, C.; Ocal, C.; Brandbyge, M.; Paulsson, M.; Sanchez-Portal, D.; Arnau, A. Exploring the Tilt-Angle Dependence of Electron Tunneling across Molecular Junctions of Self-Assembled Alkanethiols. *ACS Nano* **2009**, *3* (8), 2073−2080.
(19) Qi, Y.; Ratera, I.; Park, J. Y.; Ashby, P. D.; Quek, S. Y.; Neaton, J. B.; Salmeron, M. Mechanical and Charge Transport Properties of Alkanethiol Self-Assembled Monolayers on a Au(111) Surface: The Role of Molecular Tilt. *Langmuir* **2008**, *24* (5), 2219−2223.
(20) DelRio, F. W.; Steffens, K. L.; Jaye, C.; Fischer, D. A.; Cook, R. F. Elastic, Adhesive, and Charge Transport Properties of a Metal-Molecule-Metal Junction: The Role of Molecular Orientation, Order, and Coverage. *Langmuir* **2010**, *26* (3), 1688−1699.
(21) Meyers, M. A.; McKittrick, J.; Chen, P.-Y. Structural Biological Materials: Critical Mechanics-Materials Connections. *Science* **2013**, *339* (6121), 773−779.
(22) Tao, Y. T.; Lee, M. T.; Chang, S. C. Effect of Biphenyl and Naphthyl Groups on the Structure of Self-Assembled Monolayers: Packing, Orientation, and Wetting Properties. *J. Am. Chem. Soc.* **1993**, *115* (21), 9547−9555.
(23) Arima, Y.; Iwata, H. Effect of Wettability and Surface Functional Groups on Protein Adsorption and Cell Adhesion Using Well-Defined Mixed Self-Assembled Monolayers. *Biomaterials* **2007**, *28* (20), 3074−3082.
(24) Morin-Crini, N.; Fourmentin, M.; Fourmentin, S.; Torri, G.; Crini, G. Synthesis of Silica Materials Containing Cyclodextrin and Their Applications in Wastewater Treatment. *Environ. Chem. Lett.* **2019**, *17* (2), 683−696.
(25) Liao, R.; Lv, P.; Wang, Q.; Zheng, J.; Feng, B.; Yang, B. Cyclodextrin-Based Biological Stimuli-Responsive Carriers for Smart and Precision Medicine. *Biomater. Sci.* **2017**, *5* (9), 1736−1745.
(26) Zhang, X.; Ma, X.; Wang, K.; Lin, S.; Zhu, S.; Dai, Y.; Xia, F. Recent Advances in Cyclodextrin-Based Light-Responsive Supramolecular Systems. *Macromol. Rapid Commun.* **2018**, *39* (11), 1800142.
(27) Ulman, A. Formation and Structure of Self-Assembled Monolayers. *Chem. Rev.* **1996**, *96* (4), 1533−1554.
(28) Hughes, S. A.; Wang, F.; Wang, S.; Kreutzberger, M. A. B.; Osinski, T.; Orlova, A.; Wall, J. S.; Zuo, X.; Egelman, E. H.; Conticello, V. P. Ambidextrous Helical Nanotubes from Self-Assembly of Designed Helical Hairpin Motifs. *Proc. Natl. Acad. Sci. U. S. A.* **2019**, *116* (29), 14456−14464.
(29) Wang, H.; Xiong, W. Vibrational Sum-Frequency Generation Hyperspectral Microscopy for Molecular Self-Assembled Systems. *Annu. Rev. Phys. Chem.* **2021**, *72* (1), 279−306.
(30) Blake, M. J.; Colon, B. A.; Calhoun, T. R. Leaving the Limits of Linearity for Light Microscopy. *J. Phys. Chem. C* **2020**, *124* (45), 24555−24565.
(31) Wang, H.; Wagner, J. C.; Chen, W.; Wang, C.; Xiong, W. Spatially Dependent H-Bond Dynamics at Interfaces of Water/Biomimetic Self-Assembled Lattice Materials. *Proc. Natl. Acad. Sci. U. S. A.* **2020**, *117* (38), 23385−23392.
(32) Wang, H.; Chen, W.; Wagner, J. C.; Xiong, W. Local Ordering of Lattice Self-Assembled SDS@2β-CD Materials and Adsorbed Water Revealed by Vibrational Sum Frequency Generation Microscope. *J. Phys. Chem. B* **2019**, *123* (29), 6212−6221.
(33) Rao, Y.; Song, D.; Turro, N. J.; Eisenthal, K. B. Orientational Motions of Vibrational Chromophores in Molecules at the Air/Water Interface with Time-Resolved Sum Frequency Generation. *J. Phys. Chem. B* **2008**, *112* (43), 13572−13576.
(34) Wu, Y.; Li, W.; Xu, B.; Li, X.; Wang, H.; McNeill, V. F.; Rao, Y.; Dai, H.-L. Observation of Organic Molecules at the Aerosol Surface. *J. Phys. Chem. Lett.* **2016**, *7* (12), 2294−2297.
(35) Deng, G.-H.; Qian, Y.; Rao, Y. Development of Ultrafast Broadband Electronic Sum Frequency Generation for Charge Dynamics at Surfaces and Interfaces. *J. Chem. Phys.* **2019**, *150* (2), 024708.
(36) Watts, K. E.; Blackburn, T. J.; Pemberton, J. E. Optical Spectroscopy of Surfaces, Interfaces, and Thin Films: A Status Report. *Anal. Chem.* **2019**, *91* (7), 4235−4265.
(37) Takeshita, N.; Okuno, M.; Ishibashi, T. Molecular Conformation of DPPC Phospholipid Langmuir and Langmuir-Blodgett Monolayers Studied by Heterodyne-Detected Vibrational Sum Frequency Generation Spectroscopy. *Phys. Chem. Chem. Phys.* **2017**, *19* (3), 2060−2066.
(38) Wang, C.; Li, Y.; Xiong, W. Extracting Molecular Responses from Ultrafast Charge Dynamics at Material Interfaces. *J. Mater. Chem. C* **2020**, *8* (35), 12062−12067.
(39) Sung, W.; Müller, C.; Hietzschold, S.; Lovrinčić, R.; Gallop, N. P.; Bakulin, A. A.; Nihonyanagi, S.; Tahara, T. Preferred Orientations of Organic Cations at Lead-Halide Perovskite Interfaces Revealed Using Vibrational Sum-Frequency Spectroscopy. *Mater. Horizons* **2020**, *7* (5), 1348−1357.
(40) Elsenbeck, D.; Das, S. K.; Velarde, L. Substrate Influence on the Interlayer Electron-Phonon Couplings in Fullerene Films Probed with Doubly-Resonant SFG Spectroscopy. *Phys. Chem. Chem. Phys.* **2017**, *19* (28), 18519−18528.
(41) Gupta, P. K.; Meuwly, M. Dynamics and Vibrational Spectroscopy of Water at Hydroxylated Silica Surfaces. *Faraday Discuss.* **2014**, *167*, 329.
(42) Rao, Y.; Turro, N. J.; Eisenthal, K. B. Water Structure at Air/Acetonitrile Aqueous Solution Interfaces. *J. Phys. Chem. C* **2009**, *113* (32), 14384−14389.
(43) Zhu, X. D.; Suhr, H.; Shen, Y. R. Surface Vibrational Spectroscopy by Infrared-Visible Sum Frequency Generation. *Phys. Rev. B* **1987**, *35* (6), 3047−3050.
(44) Shen, Y. R. Surface Properties Probed by Second-Harmonic and Sum-Frequency Generation. *Nature* **1989**, *337* (6207), 519−525.
(45) Kusaka, R.; Ishiyama, T.; Nihonyanagi, S.; Morita, A.; Tahara, T. Structure at the Air/Water Interface in the Presence of Phenol: A Study Using Heterodyne-Detected Vibrational Sum Frequency Generation and Molecular Dynamics Simulation. *Phys. Chem. Chem. Phys.* **2018**, *20* (5), 3002−3009.
(46) Wanapun, D.; Kestur, U. S.; Kissick, D. J.; Simpson, G. J.; Taylor, L. S. Selective Detection and Quantitation of Organic Molecule Crystallization by Second Harmonic Generation Microscopy. *Anal. Chem.* **2010**, *82* (13), 5425−5432.
(47) Song, Z.; Sarkar, S.; Vogt, A. D.; Danzer, G. D.; Smith, C. J.; Gualtieri, E. J.; Simpson, G. J. Kinetic Modeling of Accelerated Stability Testing Enabled by Second Harmonic Generation Microscopy. *Anal. Chem.* **2018**, *90* (7), 4406−4413.
(48) Raghunathan, V.; Han, Y.; Korth, O.; Ge, N.-H.; Potma, E. O. Rapid Vibrational Imaging with Sum Frequency Generation Microscopy. *Opt. Lett.* **2011**, *36* (19), 3891.
(49) Han, Y.; Raghunathan, V.; Feng, R. R.; Maekawa, H.; Chung, C.-Y. Y.; Feng, Y.; Potma, E. O.; Ge, N.-H. H. Mapping Molecular Orientation with Phase Sensitive Vibrationally Resonant Sum-Frequency Generation Microscopy. *J. Phys. Chem. B* **2013**, *117* (20), 6149−6156.
(50) Han, Y.; Hsu, J.; Ge, N.-H.; Potma, E. O. Polarization-Sensitive Sum-Frequency Generation Microscopy of Collagen Fibers. *J. Phys. Chem. B* **2015**, *119* (8), 3356−3365.
(51) Maekawa, H.; Kumar, S. K. K.; Mukherjee, S. S.; Ge, N.-H. Phase-Sensitive Vibrationally Resonant Sum-Frequency Generation Microscopy in Multiplex Configuration at 80 MHz Repetition Rate. *J. Phys. Chem. B* **2021**, *125* (33), 9507−9516.
(52) Hsu, J.; Haninnen, A.; Ge, N.-H.; Potma, E. O. Molecular Imaging with Sum-Frequency Generation Microscopy. In *Optics in the*

Life Sciences; OSA: Washington, D.C., 2015; p NT4C.4, DOI: 10.1364/NTM.2015.NT4C.4.
(53) Potma, E. O. Advances in Vibrationally Resonant Sum-Frequency Generation Microscopy. In *Optics in the Life Sciences Congress*; OSA: Washington, D.C., 2017; p NM4C.2, DOI: 10.1364/NTM.2017.NM4C.2.
(54) Leng, C.; Hung, H.-C.; Sun, S.; Wang, D.; Li, Y.; Jiang, S.; Chen, Z. Probing the Surface Hydration of Nonfouling Zwitterionic and PEG Materials in Contact with Proteins. *ACS Appl. Mater. Interfaces* **2015**, *7* (30), 16881−16888.
(55) Kissick, D. J.; Wanapun, D.; Simpson, G. J. Second-Order Nonlinear Optical Imaging of Chiral Crystals. *Annu. Rev. Anal. Chem.* **2011**, *4* (1), 419−437.
(56) Johansson, P. K.; Koelsch, P. Label-Free Imaging of Amyloids Using Their Intrinsic Linear and Nonlinear Optical Properties. *Biomed. Opt. Express* **2017**, *8* (2), 743.
(57) Zhao, M. Hierarchical Assemblies of Polypeptoids for Rational Design of Advanced Functional Nanomaterials. *Biopolymers* **2021**, *112* (9), e23469.
(58) Lin, Q.; Owh, C.; Lim, J. Y. C.; Chee, P. L.; Yew, M. P. Y.; Hor, E. T. Y.; Loh, X. J. The Thermogel Chronicle—From Rational Design of Thermogelling Copolymers to Advanced Thermogel Applications. *Accounts Mater. Res.* **2021**, *2* (10), 881−894.
(59) He, M.; Potuck, A.; Kohn, J. C.; Fung, K.; Reinhart-King, C. A.; Chu, C.-C. Self-Assembled Cationic Biodegradable Nanoparticles from pH-Responsive Amino-Acid-Based Poly(Ester Urea Urethane)s and Their Application As a Drug Delivery Vehicle. *Biomacromolecules* **2016**, *17* (2), 523−537.
(60) Guo, Y.; Zhang, L.; Wang, K.; Yu, A.; Zhang, S.; Ouyang, G. Decorated Traditional Cellulose with Nanoscale Chiral Metal-Organic Frameworks for Enhanced Enantioselective Capture. *Chem. Commun.* **2021**, *57* (80), 10343−10346.
(61) Gong, W.; Liu, Y.; Cui, Y. Chiral and Robust Zr(iv)-Based Metal-Organic Frameworks Built from Spiro Skeletons. *Faraday Discuss.* **2021**, *231*, 168−180.
(62) Wagner, J. C.; Hunter, K. M.; Paesani, F.; Xiong, W. Water Capture Mechanisms at Zeolitic Imidazolate Framework Interfaces. *J. Am. Chem. Soc.* **2021**, *143* (50), 21189−21194.
(63) Yang, J.; Chen, M.; Lee, H.; Xu, Z.; Zhou, Z.; Feng, S.-P.; Kim, J. T. Three-Dimensional Printing of Self-Assembled Dipeptides. *ACS Appl. Mater. Interfaces* **2021**, *13* (17), 20573−20580.
(64) Chung, C.-Y.; Potma, E. O. Biomolecular Imaging with Coherent Nonlinear Vibrational Microscopy. *Annu. Rev. Phys. Chem.* **2013**, *64* (1), 77−99.
(65) Hanninen, A.; Shu, M. W.; Potma, E. O. Hyperspectral Imaging with Laser-Scanning Sum-Frequency Generation Microscopy. *Biomed. Opt. Express* **2017**, *8* (9), 4230.
(66) Katagiri, C.; Miyamae, T.; Li, H.; Yang, F.; Baldelli, S. Direct Imaging of Electric Field Behavior in 2,7-Diphenyl[1]Benzothieno-[3,2-b][1]Benzothiophene Organic Field-Effect Transistors by Sum-Frequency Generation Imaging Microscopy. *Phys. Chem. Chem. Phys.* **2021**, *23* (8), 4944−4950.
(67) Li, H.; Baldelli, S. Influence of Microcrystallinity on the CO/Pt(Poly) Electrode Surface Using Sum Frequency Generation Microscopy Combined With Electrochemistry. *J. Phys. Chem. C* **2021**, *125* (24), 13560−13571.
(68) de Lima, B. M.; Hayes, P. L.; Wood-Adams, P. M. Influence of Polymer Molecular Weight on Chain Conformation at the Polystyrene/Silver Interface. *Langmuir* **2021**, *37* (33), 10036−10045.
(69) TheElectricFlock. Neural Network Trigonometric Function. https://github.com/TheElectricFlock/Neural-Network-Trigonometric-Function (accessed Apr 12, 2021).
(70) Wang, H.-F.; Gan, W.; Lu, R.; Rao, Y.; Wu, B.-H. Quantitative Spectral and Orientational Analysis in Surface Sum Frequency Generation Vibrational Spectroscopy (SFG-VS). *Int. Rev. Phys. Chem.* **2005**, *24* (2), 191−256.
(71) Wang, H.-F.; Velarde, L.; Gan, W.; Fu, L. Quantitative Sum-Frequency Generation Vibrational Spectroscopy of Molecular Surfaces and Interfaces: Lineshape, Polarization, and Orientation. *Annu. Rev. Phys. Chem.* **2015**, *66* (1), 189−216.
(72) Rao, Y.; Comstock, M.; Eisenthal, K. B. Absolute Orientation of Molecules at Interfaces. *J. Phys. Chem. B* **2006**, *110* (4), 1727−1732.
(73) Dailey, C. A.; Burke, B. J.; Simpson, G. J. The General Failure of Kleinman Symmetry in Practical Nonlinear Optical Applications. *Chem. Phys. Lett.* **2004**, *390* (1−3), 8−13.
(74) Zhang, W.; Zheng, D.; Xu, Y.; Bian, H.; Guo, Y.; Wang, H. Reconsideration of Second-Harmonic Generation from Isotropic Liquid Interface: Broken Kleinman Symmetry of Neat Air/Water Interface from Dipolar Contribution. *J. Chem. Phys.* **2005**, *123* (22), 224713.
(75) Simpson, G. J. *Nonlinear Optical Polarization Analysis in Chemistry and Biology*; Cambridge University Press: Cambridge, U.K., 2017; DOI: 10.1017/9781139019026.
(76) Breen, P. G.; Foley, C. N.; Boekholt, T.; Zwart, S. P. Newton versus the Machine: Solving the Chaotic Three-Body Problem Using Deep Neural Networks. *Mon. Not. R. Astron. Soc.* **2020**, *494* (2), 2465−2470.
(77) Lu, L.; Jin, P.; Pang, G.; Zhang, Z.; Karniadakis, G. E. Learning Nonlinear Operators via DeepONet Based on the Universal Approximation Theorem of Operators. *Nat. Mach. Intell.* **2021**, *3* (3), 218−229.
(78) Chollet, F. Keras Neural Network Library. https://github.com/fchollet/keras (accessed Apr 12, 2021).
(79) Shah, S. A.; Baldelli, S. Chemical Imaging of Surfaces with Sum Frequency Generation Vibrational Spectroscopy. *Acc. Chem. Res.* **2020**, *53* (6), 1139−1150.
(80) Shah, S. A.; Pikalov, A. A.; Baldelli, S. ChemSpecNet: A Neural Network for Chemical Analysis of Sum Frequency Generation Spectroscopic Imaging. *Opt. Commun.* **2022**, *507*, 127691.
(81) Shah, S. A. H. Super-Resolution Imaging, Orientation Analysis, and Image Processing with Machine Learning in Sum Frequency Generation Spectroscopy. Ph.D. Thesis, University of Houston, 2020.
(82) Barrena, E.; Ocal, C.; Salmeron, M. Structure and Stability of Tilted-Chain Phases of Alkanethiols on Au(111). *J. Chem. Phys.* **2001**, *114* (9), 4210−4214.
(83) Rong, H.-T.; Frey, S.; Yang, Y.-J.; Zharnikov, M.; Buck, M.; Wühn, M.; Wöll, C.; Helmchen, G. On the Importance of the Headgroup Substrate Bond in Thiol Monolayers: A Study of Biphenyl-Based Thiols on Gold and Silver. *Langmuir* **2001**, *17* (5), 1582−1593.
(84) Buxton, G. A.; Balazs, A. C. Predicting the Mechanical and Electrical Properties of Nanocomposites Formed from Polymer Blends and Nanorods. *Mol. Simul.* **2004**, *30* (4), 249−257.
(85) Liu, Z.; Dong, B. X.; Misra, M.; Sun, Y.; Strzalka, J.; Patel, S. N.; Escobedo, F. A.; Nealey, P. F.; Ober, C. K. Self-Assembly Behavior of an Oligothiophene-Based Conjugated Liquid Crystal and Its Implication for Ionic Conductivity Characteristics. *Adv. Funct. Mater.* **2019**, *29* (2), 1805220.
(86) Niu, Y.; Pei, Y.; Ma, Y.; Li, M.; Zhang, X. Fabrication, Structural Evolutions and Properties of Large-Area Orientation Reduced Graphene Oxide Films by Self-Assembly at the Air-Water Interface and Thermal Treatment. *Mater. Lett.* **2020**, *275*, 128158.
(87) Chinwangso, P.; Lee, H. J.; Jamison, A. C.; Marquez, M. D.; Park, C. S.; Lee, T. R. Structure, Wettability, and Thermal Stability of Organic Thin-Films on Gold Generated from the Molecular Self-Assembly of Unsymmetrical Oligo(Ethylene Glycol) Spiroalkanedithiols. *Langmuir* **2017**, *33* (8), 1751−1762.
(88) Niu, Y.; Zhao, J.; Zhang, X.; Wang, X.; Wu, J.; Li, Y.; Li, Y. Large Area Orientation Films Based on Graphene Oxide Self-Assembly and Low-Temperature Thermal Reduction. *Appl. Phys. Lett.* **2012**, *101* (18), 181903.
(89) Aizawa, M.; Nakamura, H.; Matsumoto, K.; Oguma, T.; Shishido, A. Oriented Collagen Films with High Young's Modulus by Self-Assembly on Micrometer Grooved Polydimethylsiloxane. *Mater. Adv.* **2021**, *2* (21), 6984−6987.

(90) Fu, Y.; Kao, W. J. Drug Release Kinetics and Transport Mechanisms of Non-Degradable and Degradable Polymeric Delivery Systems. *Expert Opin. Drug Delivery* **2010**, *7* (4), 429−444.

https://doi.org/10.1021/acs.jpcb.2c05876
J. Phys. Chem. B 2022, 126, 7192−7201